Previously hidden landslide processes revealed using distributed acoustic sensing with nanostrain-rate sensitivity

Susanne Ouellet (susanne.ouellet2@ucalgary.ca)
University of Calgary https://orcid.org/0000-0001-8240-2916
Jan Dettmer
jan.dettmer@ucalgary.ca https://orcid.org/0000-0001-8906-8156
Matthew Lato
BGC Engineering Inc.
Steve Cole
Luna OptaSense
D. Hutchinson
Queen's University
Martin Karrenbach
Seismics Unusual Ltd.
Ben Dashwood
British Geolgoical Survey
Jonathan Chambers
British Geolgoical Survey
Roger Crickmore
Luna OptaSense

Article

Keywords:

Posted Date: January 26th, 2024

DOI: https://doi.org/10.21203/rs.3.rs-3894692/v1

Additional Declarations: There is **NO** Competing Interest.

Abstract

Landslides can sometimes creep for decades before undergoing runaway acceleration and experiencing catastrophic failure. Observing and monitoring the evolution of strain in time and space is crucial to understand landslide processes, including the transition from slow to fast movement. However, the limited spatial or temporal resolution of existing landslide monitoring instrumentation limits the study of these processes. We present a method employing distributed acoustic sensing (DAS) strain data below 1 Hertz frequency over a three-day period of rainfall and quantify strain-rate changes at meter and sub-minute scales. The results reveal rainfall-triggered landslide processes, beginning with the onset of near-surface strain changes at the head scarp. Strain acceleration at a developing rupture zone, retrogression towards the scarp and flow-lobe activity is observed as the rainfall continues. The DAS-inferred processes with displacements of less than 0.5 mm are undetected using other landslide monitoring techniques. Our method illuminates landslide processes occurring with nanostrain-rate sensitivity at spatiotemporal resolution previously not possible.

Introduction

Landslides are a major global geohazard, resulting in the loss of thousands of lives1 and an estimated average of 20 billion USD in economic losses annually2. Slow-moving landslides are associated with movement rates ranging from millimeters to several meters per year3. However, these landslides may also accelerate without apparent warning 3,4. These points highlight the unpredictability of slow-moving landslides and the importance of detecting early onset of motion and understanding their movement patterns. Furthermore, landslide risk is expected to increase due to anthropogenic factors including urbanization, deforestation and the effects of climate change (e.g. increased precipitation, permafrost degradation, wildfires)3,5–8. As settlements and infrastructure increasingly encroach upon areas with potential landslide hazards, effective monitoring systems are a critical component to support informed decisions for mitigation of landslide risk.

Landslide monitoring systems encompass a range of sensors and techniques to detect changes at Earth's surface (e.g. survey, tiltmeters, remote sensing) and at depth (e.g. inclinometer, acoustic emissions, piezometers) 9–13. Geophysical methods support landslide monitoring by inferring changes occurring at depth over broad spatial areas 14. Satellite and ground-based remote sensing technologies excel in providing broad spatial coverage and enabling landslide monitoring at sites with difficult or hazardous access. However, they are limited in capturing sudden acceleration over shorter timescales and where seasonal effects may impede measurements 3,15,16. In comparison, distributed fiber optic sensing technologies provide broad spatial coverage, but usually require more installation efforts versus remote sensing. Once installed, distributed fiber optic sensing can provide ongoing near real-time measurements17,18. Their combined high spatial and temporal resolution make them an attractive option to consider for landslide monitoring applications19,20.

Distributed acoustic sensing (DAS), also referred to as phase-sensitive optical time-domain reflectometry, is a fiber optic sensing technology relying on the phenomena of Rayleigh backscattering and is sensitive to axial strain and temperature perturbations in the fiber 19. By injecting pulses of coherent laser light into an optical fiber, an optical phase change is recorded, resulting from the backscattered light between two sections of fiber 21. As DAS permits a fiber optic cable to be repurposed into an array of broadband seismic sensors, it has effectively spurred a burgeoning field of research known as fiber-optic seismology 22–28. DAS capabilities to monitor changes at low frequencies (i.e., towards 0 Hz) are less studied. Low-frequency DAS was used to characterize hydraulic fracturing geometry, demonstrating the value in the low-frequency domain 29. Other studies, referring to a DC-coupled DAS as a distributed Rayleigh sensing system, demonstrate the capability of low-frequency DAS to measure changes in strain at the Hollin Hill Landslide Observatory 30,31.

We employ low-frequency (< 1 Hz) DAS data acquired over a three-day period and reveal the kinematics of a slow-moving landslide with nanostrain-rate sensitivity, at 1 Hz sampling and with a 4-meter spatial resolution over 925 m of optical fiber. This method provides new insights for rainfall-driven landslide motion and quantifies the spatiotemporal landslide sequence including the onset of slope movement, retrogression of the landslide and flow-lobe activity near the toe. The processes of this sequence occur at time scales of minutes and exhibit spatial patterns of meter scale. We compare the results with collocated geotechnical instrumentation to demonstrate the unparalleled spatiotemporal resolution of low-frequency DAS. Existing monitoring methods cannot resolve the observations we present. For example, monitoring methods such as ground-based interferometry and automated inclinometers (i.e., ShapeArrays) can resolve up to sub-millimeter displacements over minute timescales, but here we resolve nanostrain-rate changes with 1 Hz sampling frequency15,32.

Background

The Hollin Hill Landslide Observatory is one of the most studied slow-moving landslides in the world and has been monitored by the British Geological Survey since 2008 [3,32]. The landslide is classified as a very-slow to slow moving composite multiple earth slide–earth flow [9,33], with average velocities typically ranging from 0.5 to 3.5 m/year [9,34]. Earlier studies [9,31,34–37] divide the landslide into three major domains: the rotation-dominant domain (above mid-slope), the translation-dominant domain (mid-slope) and the flow-dominant domain (below mid-slope). Slope failure is due to the presence of very weak and highly weathered mud rocks within the landslide-prone Whitby Mudstone Formation (WMF), which outcrops on the valley side. Translational deformation of the WMF leads to rotational deformation above from unloading and oversteepening of the toe along the upper slope. The progressive displacement of the translational deformation occurs as a flow-like behavior over the Cleveland Ironstone Formation (CIF) and Staithes Sandstone Formation (SSF) below the mid-section [9].

A single-mode tight-buffered fiber-optic cable of 925 m length is buried ~ 10 cm below ground surface at the site (Fig. 1). The British Geological Survey acquired DAS data using an OptaSense ODH-F interrogator unit with a spatial sampling interval of 1 m and a spatial resolution of 4 m (i.e., gauge length) over a

three-day period in January 2021. The interrogator unit was housed in a nearby barn, located ~ 750 m from the site. The cable was buried in a shallow trench using a small backhoe and shovel, running from the interrogator housing along a farm track to the site [30]. Along the farm track, the cable was encased in protective housing and was laid bare at the site for improved coupling with the surrounding formation (**Fig. S6**). The processed six cable sections (Fig. 1A) are parallel to the direction of slope movement covering an area of ~ 135 m by 50 m. The approximate slope gradient in the instrumented area is 15 degrees. Collocated instrumentation includes piezometers, automated inclinometers (ShapeArrays) and a weather station (rain gauge, air temperature, barometric pressure) [9]. The locations of the fiber optic installation and collocated instrumentation are shown on Fig. 1. Terrestrial lidar data were acquired in November 2020 and in March 2021.

Strain perturbations along the cable result in an optical phase change $\Delta\varphi$ of the Rayleigh-backscattered light over the gauge length of the measurement, which is mapped along the axis of the fiber using principles of optical time-domain reflectometry, and has a linear relationship with strain change $\Delta\epsilon$ [20,38]

$$\Delta\epsilon = \frac{\lambda\Delta\varphi}{4\pi\zeta n L_G}$$

1

,

where *n* corresponds to a refractive index, λ corresponds to the wavelength of the coherent laser pulse and ζ corresponds to a scalar multiplicative factor to account for changes in the index of refraction (**Methods**).

We apply a 1-Hz low-pass filter, then convert the optical phase data to units of strain and strain rate. The resulting spatiotemporal images of strain rate along the six processed cable sections reveal complex patterns of accelerating and decelerating strain at the site. Cable sections are labelled from west to east as L1 to L6. We also infer landslide displacements and velocities from the DAS strain and strain-rate data (**Methods**) and quantitatively compare those inferences with collocated geotechnical instrumentation.

We employ these low-frequency DAS measurements to interpret spatiotemporal patterns of strain-rate transients at the Hollin Hill site over a period of intense rainfall. Our results highlight landslide processes at scales previously unresolved, enabling new insights into the kinematic evolution of slow-moving landslides.

Results

With one-minute temporal resolution (based on the median filter, see **Methods**), four-meter spatial resolution (akin to the gauge length) and nanostrain-rate sensitivity, we develop strain-rate spatiotemporal images (Fig. 2) with an unprecedented level of detail to assess evolving changes at the near-surface compared to remote sensing methods [15].

Rainfall occurred over a 1.5-day period (January 13 at noon to January 14 at 18:30) with a cumulative precipitation of 28 mm. We develop a conceptual model to illustrate key areas where noteworthy changes in strain and strain rate are observed. We observe a sequence of interrelated events demonstrating: (1) initiation of strain at the head scarp, (2) subsequent triggering of a rupture zone, (3) retrogressive strain towards the scarp and flow lobe surge, and (4) stabilization of the rupture zone with a gradual increase in strain at the scarp (Sequences 1 through 4). The unparalleled spatiotemporal resolution of our findings reveals how a complex slow-moving landslide evolves through time and space.

Strain initiation at head scarp (Sequence 1)

The initial onset of strain is observed after about eight hours of rainfall at the northeast corner of the array at the scarp (Fig. 2). Over the subsequent eight-hour period, we observe a steady increase in strain near the main scarp, with an average inferred velocity of 1 mm per day (Fig. 3B). This corresponds with a steady increase in soil moisture content from 43 to 47%.

Triggering of rupture zone (Sequence 2), retrogression towards scarp (Sequence 3A) and flow lobe surge (Sequence 3B)

From 03:00 to 10:00 on January 14, the rupture zone, located ~ 30 m southwest of the main scarp develops increasing strain centered around cable section L4. The strain accelerates to a maximum inferred velocity of 12 mm/day at 12:00 on January 14 (Fig. 3A, Sequence 2). Over this period, the soil moisture content increases from 47% to a maximum of 53%. Here, a general retrogression of the rupture zone towards the scarp occurs (Sequence 3A). We estimate an average retrogression velocity of ~ 1.7 m/hour, as the strain-rate front propagates over a 20-m distance in a 12-hour period. This coincides with accelerating strain near the main scarp. Further downslope, propagation of the strain front at the flow lobe occurs across ~ 10 m in the downslope direction over a four-hour period (~ 2.5 m/hour; **Fig. S1**, Sequence 3B). We interpret this rapid movement as a surge of superficial material flowing over the cable (not representative of the motion of the rupture zone assessed above, where the material is assumed to be well coupled with the cable, see **Discussion**).

Stabilization of rupture zone with gradual deceleration in strain at scarp (Sequence 4).

The final sequence coincides with a stabilization of the rupture zone, where the strain rate approaches near zero values (Figs. 2 and 3A). A maximum strain of ~ 1,000 microstrain occurs at the rupture zone on January 14 at 22:00, ~ 12 hours following the highest intensity rainfall and remains at near-constant strain levels after the rain subsides. The soil moisture content decreases to 43%. Meanwhile, the strain continues to increase at more gradual levels at the main scarp up until the end of the DAS acquisition period (< ~ 1 mm per day).

Further to the above, historical satellite imagery shows the westward propagation of the landslide and the development of the main scarp, occurring following major movement in 2016 [14]. With data acquisition over only a three-day period, our results show that the landslide is continuing to propagate westward,

considering the maximum strain changes in the rupture zone to the west of the existing scarp (Figs. 2, 4 and 6).

Assessment of DAS-derived displacements with geotechnical instrumentation

We rely on collocated geotechnical instrumentation to evaluate the inferred displacements from DAS strain. Our comparison provides evidence for the reliability of the relative magnitudes of the DAS strain-rate, strain and inferred displacements. Furthermore, it illustrates the low noise levels at a single DAS channel in comparison with the ShapeArray, permitting unprecedented resolution of changes in movement to be detected.

We compare relative displacement data from two vertical ShapeArrays installed near the fiber optic cable array to a depth of 2.5 m, at the west flow lobe and east flow lobe in 2013 (Fig. 5). The near-surface (~ 0.3-m depth) ShapeArray data are processed to obtain relative displacement from a common baseline for comparison with the inferred DAS displacement (**Methods**). Generally, higher magnitudes of both ShapeArray and DAS data are observed at the west lobe. The total displacement at the east-lobe and west-lobe ShapeArrays are 0.6 mm and 0.8 mm, respectively. The DAS-derived displacements at nearby locations vary from 0.3 mm (between east and west lobes) to 0.4 mm (adjacent to west-lobe ShapeArray). The observed discrepancies are likely a result of: (1) the accuracy and precision of the ShapeArray data at very small (< 1 mm) displacements, and (2) the strain transfer occurring inside the fiber-optic cable and the coupling of the cable to the surrounding ground; and (3) the different depths of measurement and sensor locations. The observed variability between subsequent ShapeArray samples (+/- ~0.1 mm) illustrates higher noise in comparison with the DAS estimates (Fig. 5**).** As the strain is enclosed within a fiber-optic cable comprising multiple layers with imperfect coupling to the surrounding ground, this results in a lower strain in the core versus the strain in the surrounding ground [39,40]. The temporal changes in displacement are well correlated, with the main increase in strain observed to occur on January 14 at noon in both the ShapeArray and DAS data.

Discussion

Our method can infer slow variances in millistrain over days to fast changes of strain-rate fronts propagating at 2.5 m/hour from low frequency DAS data. This new capability enables landslide monitoring on spatiotemporal scales that are currently poorly understood. We can distinguish kinematic zones which vary over time to support landslide hazard assessments[41]. For example, the motion characteristics of slower soil-creep events are discerned from more rapid flow-surge events. Importantly, this addresses existing limitations of state-of-the-art remote sensing technologies such as ground-based interferometry and Doppler radar[15] which lack temporal resolution and sensitivity to small displacements. Therefore, our DAS-based method can provide crucial information for landslide early-warning applications.

The initial strain change is observed at the northeast corner of the array at the location of the main scarp. This is likely a result of the main scarp providing a direct rainfall-infiltration pathway to the near-surface cable. Similar to the observations described by [42], rainfall-induced saturation of the soil at the depth of the cable is believed to decrease the friction between the cable and surrounding ground, resulting in a small decrease in strain. Although the strain-rate changes show visible activity at the scarp, the overall change in strain in the northeast corner of the array remains negligible in this early period in comparison with the maximum strain changes occurring after sustained rainfall. This highlights a major advantage of using strain-rate data alongside strain to help distinguish the onset of changes. For landslide early-warning applications, DAS strain rates (and the inferred velocities) could become an important tool to enable monitoring over broad temporal and spatial scales [3,15,43].

Following the onset of strain, development of a rupture zone to the south of the scarp becomes apparent. We do not observe a continuous propagation of strain between the location of the scarp and the initial zone of rupture (Fig. 4 at 2021-01-14T10:00). This is likely a result of our interpreted rotational slip-surface geometry, where the greatest observed tensile strains at the near-surface cable are expected to occur where the slip surface intersects with the cable. We observe compressive strains at the toe of the interpreted rotational failure, followed by tensile strain at the scarp, suggesting retrogression of the slope. As the slide retrogresses towards the scarp, the strain between these two locations increases as expected with our conceptual model (Fig. 4 at 2021-01-14T15:00). The tensile and compressive strains at the main rupture zone indicate likely slip surface entry and exit points. Overall, the distribution of positive and negative strains aligns with our interpretation of the main landslide processes.

The complex spatiotemporal patterns represent an important insight into landslide behaviour occurring over shorter timescales, as our results represent activity over a three-day period. The spatiotemporal DAS images and complementary geotechnical data support our interpretation of the sequential occurrence of events and active areas of movement. The DAS data reveal changes in displacement of < 1 mm that correlate with ShapeArray data, further highlighting how DAS data can complement slope monitoring networks. Our observations are consistent with earlier studies[34,35] that demonstrate the influence of seasonal precipitation on slope movement. A longer data acquisition period is recommended to understand how the strain-rate patterns evolve over longer time periods (i.e., months to years) (**Fig. S3**).

Distributed fiber optic sensing (DFOS) technologies are primarily sensitive to changes occurring along the axial direction of the optical fiber. As such, strain changes along a slip surface at depth (where the direction of movement is not aligned with the cable) could be masked. This raises a significant consideration for the cable installation geometry in future experiments. Ideally, the cable should be aligned for maximum sensitivity with changes (parallel to the direction of slope movement). Additional cable geometries, orthogonal to the direction of slope movement, could also be used to support characterization of multi-directional landslide movement patterns. For rotational failure surfaces, the DAS sensitivity to strain changes will vary dependent on the difference in angle between the slip surface and the cable. However, others [40,44] have shown that DFOS can still be used successfully to detect and monitor the development of landslide shear zones over time, even in situations where the shear zone is

perpendicular to the cable (e.g., when the cable is installed down a borehole). Future research should investigate the effect of cable geometry on the detectable strain thresholds. Regardless, our experiment demonstrates the valuable insights gleaned from a near-surface trench installation.

We assume the cable is relatively well coupled to the ground for the entirety of the acquisition period, except for the flow-lobe activity where superficial material flows over the cable (**Results** and **Fig. S1**). A laboratory-scale failure with a distributed strain sensing technology demonstrates the different phases of strain detection [42]. The authors highlight a period of partial coupling followed by full decoupling to illustrate how the strain is no longer representative of the ground strain following decoupling. As the Hollin Hill site does not undergo a major failure (the ~ 1 mm of deformation is relatively minor in comparison with earlier and subsequent movements, **Fig. S3**), we believe our assumptions of good coupling between the cable and the surrounding ground over the acquisition period are reasonable. Furthermore, the steady strains observed at most channels support our claim of negligible slippage or decoupling. However, pullout experiments could support future experiments and monitoring activities with DAS by providing an estimate of the maximum strain that can be experienced by the cable prior to likely decoupling, as demonstrated in [42]. Our comparison with nearby ShapeArray instrumentation provide us with a simplified approach to estimating the strain transfer between the optical fiber and surrounding formation. In general, the displacement magnitudes from the ShapeArray instrumentation are twice the magnitudes of inferred displacement from the nearby DAS channels. This relationship between ground displacement from ShapeArray instrumentation and DAS inferred displacement can be extended to estimate a strain transfer of 0.5, under the assumption of similar coupling throughout the fiber optic cable array.

As the velocity of slow-moving landslides can vary significantly over both time and space, an effective landslide monitoring system should be capable of capturing both longer-term changes in trend and the potential for accelerating conditions leading to a catastrophic failure over the landslide extents [3,15]. Our work demonstrates the capabilities of DAS in resolving highly sensitive changes in both time and space to uncover landslide processes not previously known. Landslide forecasting methods commonly rely on displacement monitoring as the primary indicator to inform the time of failure [43,45–47]. Although forecasting time to failure was outside the scope of this work, similar methods could also be applied using DAS strain and strain-rate data for landslide monitoring applications.

Over a three-day period encompassing high-intensity rainfall, we quantify the kinematics of the spatiotemporal landslide sequence from DAS strain and strain-rate changes. Our findings reveal landslide processes including strain onset, retrogression, and flow-lobe activity, with less than minute temporal resolution and nanostrain-rate sensitivity. Although this study relies on the low frequencies (< 1Hz) from a DAS dataset, DAS fiber-optic sensing also provides rich information at higher frequencies [22,23,48–50] which may enable further discoveries about landslides. This opens new research avenues to explore for landslide monitoring, by pairing seismic monitoring with the static strain-change monitoring we presented here. Since DAS monitoring of tens of kilometers of fibre is common, the method we presented could

effectively complement existing remote sensing techniques and be employed in early warning systems due to its low computational cost and DAS systems' ability to transmit data in real-time [25–27,51,52]. Considering the increasing frequency of landslides driven by climate change [5,53], our DAS method could provide critical information for slope stability monitoring in densely populated areas.

Materials and Methods

DAS relies on Rayleigh light backscattering, where small-scale variations in the fiber's refractive index, due to its crystalline structure, allow for Rayleigh backscattering to occur. The phase of the backscattered light is altered where there are localized disturbances to the fiber. By measuring the difference in phase between two sections of the fiber, a signal is obtained that can be converted to a strain or strain rate for output, using the speed of light and known properties of the fiber [22,54]. As such, DAS does not measure absolute strain, but instead measures relative change in strain dependent on the optical phase change attributed to a disturbance in the fiber [21]. The DAS measurement corresponds to a discrete point (i.e. channel) along the fiber, representing an average measurement over a length of fiber referred to as the gauge length (L_G) [49,55] (Fig. 7).

The output of DAS is dependent on the type of interrogator employed. For this experiment, the raw DAS output was provided in units of optical phase change (Δφ) and can be linearly related to the average strain change ($\Delta\varepsilon$) along the axis of the fiber over the gauge length L_G (Eq. (1); [23]). For this study, n corresponds to a refractive index of 1.468 for the single mode fiber, L_G corresponds to a gauge length of 4.084 m, λ corresponds to the wavelength of the coherent laser pulse in a vacuum of 1550.12 nm and ξ corresponds to a scalar multiplicative factor of 0.81, accounting for changes in the index of refraction. Separate from the gauge length, the channel spacing determines the spatial distance between each sample along the optical fiber (Fig. 7). Selecting a channel spacing less than the L_G is akin to applying a moving average filter to the dataset.

As the output from DAS is represented as an average strain change $\Delta\epsilon$ over the gauge length, displacement d is inferred by integrating the average strain change over the gauge length L_G

$$d = \Delta\epsilon L_G$$

2

Change in strain rate is obtained by performing a temporal derivative on the average strain change $\Delta\epsilon$

$$\dot{\epsilon} = \frac{d\Delta\epsilon}{dt}$$

3

Velocity v is inferred by integrating the average change in strain rate $\dot{\epsilon}$ over the gauge length L_G

$$v = \dot{\epsilon} L_G$$

4

Although most geotechnical studies involving DAS to date focus on its applications as a seismic sensor [56–58], we focus on low frequency (< 1 Hz) DAS measurements to extract meaningful information on changes in static strains. This was first demonstrated by [29], who used low frequency DAS to measure small changes in strain for hydraulic fracturing applications. Here, we extend the application of low frequency DAS towards a slow-moving landslide using a tight-buffered fiber optic cable. The following data processing steps are implemented to obtain low frequency DAS strain, displacement, strain rate and velocity measurements.

1. DAS data are acquired using the OptaSense ODH-F interrogator unit in the quantitative mode. The obtained data represent the optical phase change at a sampling rate of 500 Hz. Data are acquired in a proprietary file format. They are decimated to 50 Hz with a low-pass anti-aliasing filter and exported to HDF5 file format using the OptaSense DxS software. The remainder of the data processing steps are completed using the following open-source Python modules: SciPy [60], NumPy [61], Pandas, H5Py, Obspy, Zarr and Xarray [62].
2. The DAS data are decimated to 1 Hz following the application of a low-pass antialiasing filter.
3. Optical phase data are converted to strain using Eq. 1.
4. Relative strain measurements are obtained by subtracting subsequent samples from the initial sample at time 2021-01-12T11:38:10 for each DAS channel. No median filter is implemented on the strain data.
5. Strain-rate data are obtained by computing the temporal derivative of strain using the central differences method between consecutive samples (Eq. 3).
6. A 2D median filter is implemented on the strain-rate data, using a window size of 3 channels and 59 seconds, with zero-padding on data extents.
7. Displacement and velocity data are inferred by integrating the strain and strain-rate data over the gauge length, respectively (Equations 2 and 4).

The locations and elevations of the fiber optic cable array were collected using a Leica Viva GS14 antenna and CS15 handset at 20-m intervals. Linear interpolation between each as-built location was used to infer location data at each DAS channel. Short periods of data gaps visible in Figs. 2, 3 and 5 are due to corrupt raw data files, attributed to power-related issues during the data acquisition. Complementary geotechnical site data used to support our interpretation are described in the following paragraphs.

Weather Station

A weather station, installed in 2008 [9], records soil moisture with a sensor installed at 0.1-m depth and rainfall data recorded at 30-minute intervals (Fig. 1). Data from this weather station is publicly available as part of the UK Centre for Ecology and Hydrology [62].

Displacement measurements (ShapeArray): ShapeArrays (also known as Shape Acceleration Arrays; SAAs) were installed in 2013 and have been providing near continuous measurements since that time [9]. ShapeArrays consist of an array of micro electro mechanical system (MEMS) accelerometers. These instruments measure the acceleration relative to gravity in the x-, y- and z- directions at rigid segments along the length of the instrument to obtain a tilt measurement at each segment. Using a fixed reference point, relative displacements can be calculated from the tilt data [63]. ShapeArrays were installed to depths of ~ 2.5 m below ground level with 0.25-m sensor spacing. Instruments were assumed to be installed with the x-direction oriented horizontally parallel to the direction of movement along the downslope axis. In comparison, the DAS represents axial strain along the direction of the cable, parallel to the slope (average slope gradient of 15°). To account for the difference in magnitude of a displacement along the horizontal axis recorded by the ShapeArray and at a slope gradient of 15° recorded by DAS, a correction factor of 0.97 (cos 15°) could be implemented. For this work, we do not implement a correction factor as 0.97 is negligible for our purposes. However, we note that this should be considered for future experiments with greater slope gradients comparing DAS and ShapeArray data. Over the DAS acquisition period, the ShapeArrays acquired data with a varying sample interval between 30-minutes to one hour). The west lobe ShapeArray was not recording data from January 14 at 11:00 to January 15 at 13:00 for reasons unknown. To compare the ShapeArray data with the DAS data, we selected a common baseline reference to review relative displacement. We selected the closest available time (January 12 at 12:00) based on the ShapeArray sampling interval to the beginning of the DAS recording (January 12 at 11:38). The x-direction displacement at the shallowest sensor (at ~ 0.3-m depth) was selected for comparison with DAS. A full depth profile of the west lobe and east lobe ShapeArrays is included in Figure S4, illustrating changes over the three-day period. Based on the lateral deformation along the ShapeArray installation depth, we observe an initiation of movement at 1.5 m depth at the west lobe ShapeArray, and at 1.0 m depth at the east lobe ShapeArray. Deformation is observed to be distributed towards the surface. We select two DAS channels at adjacent cable sections closely aligned with the ShapeArrays for comparison.

Temperature effects:

In addition to strain changes, temperature changes also cause a linear change in the optical phase change $\Delta\phi$ recorded by DAS [64–66]. This can be represented using the DAS thermal coefficient C_T and the DAS strain coefficient C_ϵ [64], where

$$\Delta\phi = C_T\Delta T + C_\epsilon\Delta\epsilon$$

5

We estimate the influence of temperature changes on our DAS data by using a nearby temperature sensor installed at the fiber optic cable depth (10 cm below ground surface). The temperature sensor is installed at the location of the weather station (Fig. 1A). We follow the approach described by [64] to compute the

equivalent strain for the general temperature change of 1.7°C (**Fig. S5**) occurring over our DAS acquisition period. The DAS thermal (C_T) and strain (C_ϵ) coefficients using Eqs. 6 and 7.

$$C_T = \frac{4\pi n L_G}{\lambda}\left(\frac{\xi_T}{n} + \frac{\xi_\epsilon}{n}\alpha + \alpha\right)$$

6

$$C_\epsilon = \frac{4\pi n L_G}{\lambda}\left(1 + \frac{\xi_\epsilon}{n}\right)$$

7

The variables used to obtain C_T and C_ϵ are outlined in Table 1.

Table 1
Properties of single mode optical fiber and DAS data acquisition settings.

Variable	Symbol	Value	Units	Reference
Thermo-optic coefficient	ξ_T	$1.20{\cdot}10^{-5}$	1/°C	67
Strain-optic coefficient	ξ_ϵ	-0.32	1/strain	67
Thermal expansion coefficient	α	$8.00{\cdot}10^{-7}$	1/°C	67
Wavelength	λ	1550.12	nm	DAS acquisition settings
Index of refraction	n	1.468	Dimensionless	67
Gauge length	L_G	4.08	meters	DAS acquisition settings

Temperature and strain are represented as average values over the gauge length of 4.1 m. The DAS thermal and strain coefficients were computed as 427 radians/°C and $3.8{\cdot}10^7$ radians/strain. As such, a change in 1°C corresponds to change of $1.1{\cdot}10^{-5}$ (equivalent to 11 microstrain). We used a temperature sensor (installed at the weather station (Fig. 1A) at 10 cm depth) to estimate the relative contribution of temperature changes on the optical phase data. Over the three-day DAS data acquisition period, the ground temperature decreased by about 1.7 °C (**Fig. S5**). This change can be converted into an equivalent strain of $1.84{\cdot}10^{-5}$ m/m. This value is approximately two orders of magnitude lower than the main strain changes observed over the rainfall period that were used to inform our conceptual model (**Fig. S2**). As such, we deem it reasonable to neglect the effects of temperature in our work. However, incorporating the effects of temperature change could be used to increase the DAS measurement precision at lower strains.

Declarations

Acknowledgments

The authors gratefully acknowledge the support of industry partners on this research, made possible under a Mitacs Accelerate International grant. BGC Engineering and OptaSense acted as the industry sponsors of this research project and provided technical review and support. We thank Andres Chavarria and Victor Yartsev of OptaSense for providing technical support and for sharing the collected DAS dataset jointly with the British Geological Survey. We thank OptaSense and the Norwegian Geotechnical Institute for hosting the first author for two research visits where much of the data analysis and writing was advanced. We thank Angela Küpper of BGC Engineering, Dylan Mikesell, Sparsha Nagula, and Luca Piciullo of the Norwegian Geotechnical Institute for many insightful discussions. The British Geological Survey shared the collocated instrumentation data and lidar scans. Ben Dashwood and Jonathan Chambers publish with the permission of the Executive Director, British Geological Survey (UKRI-NERC). We are grateful for invaluable review comments provided by Andreas Fichtner and two anonymous reviewers on an earlier version of this manuscript.

Funding:

Mitacs Accelerate International grant IT31799 (JD)

Author contributions:

Conceptualization: SO, JD, JH

Methodology: SO, JD

Investigation: SC, RC, BD, JC

Visualization: SO, ML

Supervision: JD

Writing—original draft: SO

Writing—review & editing: SO, JD, ML, MK, JH, RC, SC, BD, JC

Competing interests:

Authors declare that they have no competing interests.

Data and materials availability: The relevant data to reproduce the results of this research have been uploaded to a public repository and is available at: 10.5281/zenodo.8356348.

Supplementary Materials

Figs. S1 to S6

References

1. Petley D (2012) Global patterns of loss of life from landslides. Geology 40:927–930
2. Sim K, Ben, Lee ML, Wong SY (2022) A review of landslide acceptable risk and tolerable risk. *Geoenvironmental Disasters* vol. 9 Preprint at https://doi.org/10.1186/s40677-022-00205-6
3. Lacroix P, Handwerger AL, Bièvre G (2020) Life and death of slow-moving landslides. *Nature Reviews Earth and Environment* vol. 1 404–419 Preprint at https://doi.org/10.1038/s43017-020-0072-8
4. Palmer J (2017) Palmer 2017 creeping earth secret to deadly landslides 548384a. Nat News Feature 548:384–386
5. Huggel C, Clague JJ, Korup O (2012) Is climate change responsible for changing landslide activity in high mountains? Earth Surf Process Landf 37:77–91
6. Petley D (2010) On the impact of climate change and population growth on the occurrence of fatal landslides in South, East and SE Asia. Q J Eng GeolHydrogeol 43:487–496
7. Handwerger AL, Huang MH, Fielding EJ, Booth AM, Bürgmann R (2019) A shift from drought to extreme rainfall drives a stable landslide to catastrophic failure. Sci Rep 9,
8. White RH et al (2023) The unprecedented Pacific Northwest heatwave of June 2021. Nat Commun 14,
9. Uhlemann S et al (2016) Assessment of ground-based monitoring techniques applied to landslide investigations. Geomorphology 253:438–451
10. Dixon N et al (2018) An acoustic emission landslide early warning system for communities in low-income and middle-income countries. Landslides 15:1631–1644
11. Stähli M et al (2014) Monitoring and prediction in Early Warning Systems (EWS) for rapid mass movements. Nat Hazards Earth Syst Sci Discuss 2:7149–7179
12. Pecoraro G, Calvello M, Piciullo L (2019) Monitoring strategies for local landslide early warning systems. *Landslides* vol. 16 213–231 Preprint at https://doi.org/10.1007/s10346-018-1068-z
13. Macciotta R, Hendry M, Martin CD (2016) Developing an early warning system for a very slow landslide based on displacement monitoring. Nat Hazards 81:887–907
14. Whiteley JS, Chambers JE, Uhlemann S, Wilkinson PB, Kendall JM (2019) Geophysical Monitoring of Moisture-Induced Landslides: A Review. *Reviews of Geophysics* vol. 57 106–145 Preprint at https://doi.org/10.1029/2018RG000603
15. Casagli N, Intrieri E, Tofani V, Gigli G, Raspini F (2023) Landslide detection, monitoring and prediction with remote-sensing techniques. Nat Rev Earth Environ 4:51–64
16. Petley DN, Mantovani F, Bulmer MH, Zannoni A (2005) The use of surface monitoring data for the interpretation of landslide movement patterns. Geomorphology 66:133–147

17. Lior I et al (2021) On the Detection Capabilities of Underwater Distributed Acoustic Sensing. J Geophys Res Solid Earth 126,
18. Forbes B, Ouellet S, Suszek N, Lato M, Russell B (2021) Application of distributed acoustic sensing within a tailings dam warning system. in *Proceedings of Tailings and Mine Waste* 469–477
19. Bao X, Wang Y (2021) Recent Advancements in Rayleigh Scattering-Based Distributed Fiber Sensors. *Advanced Devices & Instrumentation* (2021)
20. Bao X, Chen L (2012) Recent Progress in Distributed Fiber Optic Sensors. *Sensors (Switzerland)* vol. 12 8601–8639 Preprint at https://doi.org/10.3390/s120708601
21. Masoudi A, Newson TP (2016) Contributed Review: Distributed optical fibre dynamic strain sensing. Rev Sci Instrum 87,
22. Lindsey NJ, Martin ER (2021) Fiber-Optic Seismology. Annu Rev Earth Planet Sci 49:309–336
23. Lindsey NJ, Rademacher H, Ajo-Franklin JB (2020) On the Broadband Instrument Response of Fiber-Optic DAS Arrays. J Geophys Res Solid Earth 125,
24. Lindsey NJ et al (2017) Fiber-Optic Network Observations of Earthquake Wavefields. Geophys Res Lett 44, 11,792 – 11,799
25. Dou S et al (2017) Distributed Acoustic Sensing for Seismic Monitoring of the Near Surface: A Traffic-Noise Interferometry Case Study. Sci Rep 7,
26. Ajo-Franklin JB et al (2019) Distributed Acoustic Sensing Using Dark Fiber for Near-Surface Characterization and Broadband Seismic Event Detection. Sci Rep 9,
27. Tribaldos VR *Surface Wave Imaging using Distributed Acoustic Sensing Deployed on Dark Fiber: Moving Beyond High Frequency Noise*
28. Zhan Z (2019) Distributed acoustic sensing turns fiber-optic cables into sensitive seismic antennas. Seismol Res Lett 91:1–15
29. Jin G, Roy B (2017) Hydraulic-fracture geometry characterization using low-frequency das signal. Lead Edge 36:975–980
30. Clarkson P et al (2022) Interpretation of Distributed Rayleigh Sensing Data for Slope Stability and Ground Condition Monitoring. in *11th International Symposium on Field Monitoring in Geomechanics* (ed. Ridley, A.)
31. Clarkson P et al (2022) American Rock Mechanics Association,. Verification of a distributed fiber optic sensing slope stability monitoring solution. in *Proceedings of the 56th US Rock Mechanics/Geomechanics Symposium*
32. Chambers J et al (2022) Long-term geoelectrical monitoring of landslides in natural and engineered slopes. Lead Edge 41:768–767
33. Cruden DM, Varnes DJ (1996) *Monitoring strategies for enhanced landslide understanding and safety View project Sensitive clay landslides View project*. Natl Acad Sci Special Rep vol. 247 https://www.researchgate.net/publication/269710331

34. Uhlemann S et al (2017) Four-dimensional imaging of moisture dynamics during landslide reactivation. J Geophys Res Earth Surf 122:398–418
35. Boyd J et al (2021) A linked geomorphological and geophysical modelling methodology applied to an active landslide. Landslides 18:2689–2704
36. Gunn DA et al (2013) Rapid observations to guide the design of systems for long-term monitoring of a complex landslide in the upper lias clays of North Yorkshire, UK. Q J Eng GeolHydrogeol 46:323–336
37. Merritt AJ et al (2014) 3D ground model development for an active landslide in Lias mudrocks using geophysical, remote sensing and geotechnical methods. Landslides 11:537–550
38. Bao X, Wang Y (2021) Recent Advancements in Rayleigh Scattering-Based Distributed Fiber Sensors. *Advanced Devices & Instrumentation* (2021)
39. Soga K, Luo L (2018) Distributed fiber optics sensors for civil engineering infrastructure sensing. J Struct Integr Maintenance 3:1–21
40. Acharya A, Kogure T (2023) Application of novel distributed fibre-optic sensing for slope deformation monitoring: a comprehensive review. *International Journal of Environmental Science and Technology* vol. 20 8217–8240 Preprint at https://doi.org/10.1007/s13762-022-04697-5
41. Hungr O, Leroueil S, Picarelli L (2014) The Varnes classification of landslide types, an update. *Landslides* vol. 11 167–194 Preprint at https://doi.org/10.1007/s10346-013-0436-y
42. Schenato L et al (2017) Distributed optical fibre sensing for early detection of shallow landslides triggering. Sci Rep 7,
43. Intrieri E, Carlà T, Gigli G (2019) Forecasting the time of failure of landslides at slope-scale: A literature review. *Earth-Science Reviews* vol. 193 333–349 Preprint at https://doi.org/10.1016/j.earscirev.2019.03.019
44. Kogure T, Okuda Y (2018) Monitoring the Vertical Distribution of Rainfall-Induced Strain Changes in a Landslide Measured by Distributed Fiber Optic Sensing With Rayleigh Backscattering. Geophys Res Lett 45:4033–4040
45. Fukuzono T (1985) A Method to Predict the Time of Slope Failure Caused by Rainfall Using the Inverse Number of Velocity of Surface Displacement. J Japan Landslide Soc 22:8–14
46. Voight BA (1988) Relation to Describe Rate-Dependent Material Failure. Sci (1979) 243:200–203
47. Saito M (1965) Forecasting the Time of Occurence of a Slope Failure. Int Soc Soil Mech Geotech Eng
48. Fang G, Li YE, Zhao Y, Martin ER (2020) Urban Near-Surface Seismic Monitoring Using Distributed Acoustic Sensing. Geophys Res Lett 47,
49. Karrenbach M et al (2019) Fiber-optic distributed acoustic sensing of microseismicity, strain and temperature during hydraulic fracturing. Geophysics 84:D11–D23
50. Paitz P et al (2021) Empirical investigations of the instrument response for distributed acoustic sensing (Das) across 17 octaves. Bull Seismol Soc Am 111:1–10

51. Yu C, Zhan Z, Lindsey NJ, Ajo-Franklin JB, Robertson M (2019) The Potential of DAS in Teleseismic Studies: Insights From the Goldstone Experiment. Geophys Res Lett 46:1320–1328
52. Martin ER et al (2016) Interferometry of a roadside DAS array in Fairbanks, AK.
53. Intergovernmental Panel on Climate Change (IPCC) (2022) High Mountain Areas. The Ocean and Cryosphere in a Changing Climate. Cambridge University Press, pp 131–202. doi:10.1017/9781009157964.004.
54. Hartog A, Frignet B, Mackie D, Clark M (2014) Vertical seismic optical profiling on wireline logging cable. Geophys Prospect 62:693–701
55. Martin ER, Lindsey NJ, Ajo-Franklin JB, Biondi B (2021) Introduction to Interferometry of Fiber Optic Strain Measurements. in *Distributed Acoustic Sensing in Geophysics: Methods and Applications* (eds. Li, Y., Karrenbach, M. & Ajo-Franklin, J.) 1–33 (John Wiley & Sons,
56. Rossi M, Wisén R, Vignoli G, Coni M (2022) Assessment of Distributed Acoustic Sensing (DAS) performance for geotechnical applications. Eng Geol 306,
57. Ravet F, Briffod F, Goy A, Rochat E (2021) Mitigation of geohazard risk along transportation infrastructures with optical fiber distributed sensing. J Civ Struct Health Monit 11:967–988
58. Niu Y, Chian SC, Li YE, Fang G (2023) Laboratory Small-Strain Stiffness Measurement Using Distributed Acoustic Sensing. Geotech Test J 46:20220204
59. Virtanen P et al (2020) SciPy 1.0: fundamental algorithms for scientific computing in Python. Nat Methods 17:261–272
60. Harris CR et al (2020) Array programming with NumPy. *Nature* vol. 585 357–362 Preprint at https://doi.org/10.1038/s41586-020-2649-2
61. Hoyer S, Hamman J, xarray (2017) N-D labeled Arrays and Datasets in Python. J Open Res Softw 5:10
62. UK Centre for Ecoloy and Hydrology. COSMOS UK Site: Hollin Hill. https://cosmos.ceh.ac.uk/sites/HOLLN
63. Yan R, Take WA, Hoult NA, Meehan J, Levesque C (2021) Evaluation of Shape Array sensors to quantify the spatial distribution and seasonal rate of track settlement. Transp Geotechnics 27,
64. Leggett SE, Zhu D, Hill AD (2022) *Thermal Effects on Far-Field Distributed Acoustic Strain-Rate Sensors*. *SPE Journal* http://onepetro.org/SJ/article-pdf/27/02/1036/2688506/spe-205178-pa.pdf/1
65. Lauber T, Lees G (2021) Enhanced Temperature Measurement Performance: Fusing DTS and das Results. IEEE Sens J 21:7948–7953
66. Sidenko E, Tertyshnikov K, Lebedev M, Pevzner R (2022) Experimental study of temperature change effect on distributed acoustic sensing continuous measurements. Geophysics 87,
67. Carr JJ, Saikkonen SL, Williams DH (1990) Refractive index measurements on single-mode fiber as functions of product parameters, tensile stress, and temperature. Fiber Integr Opt 9:393–396

Figures

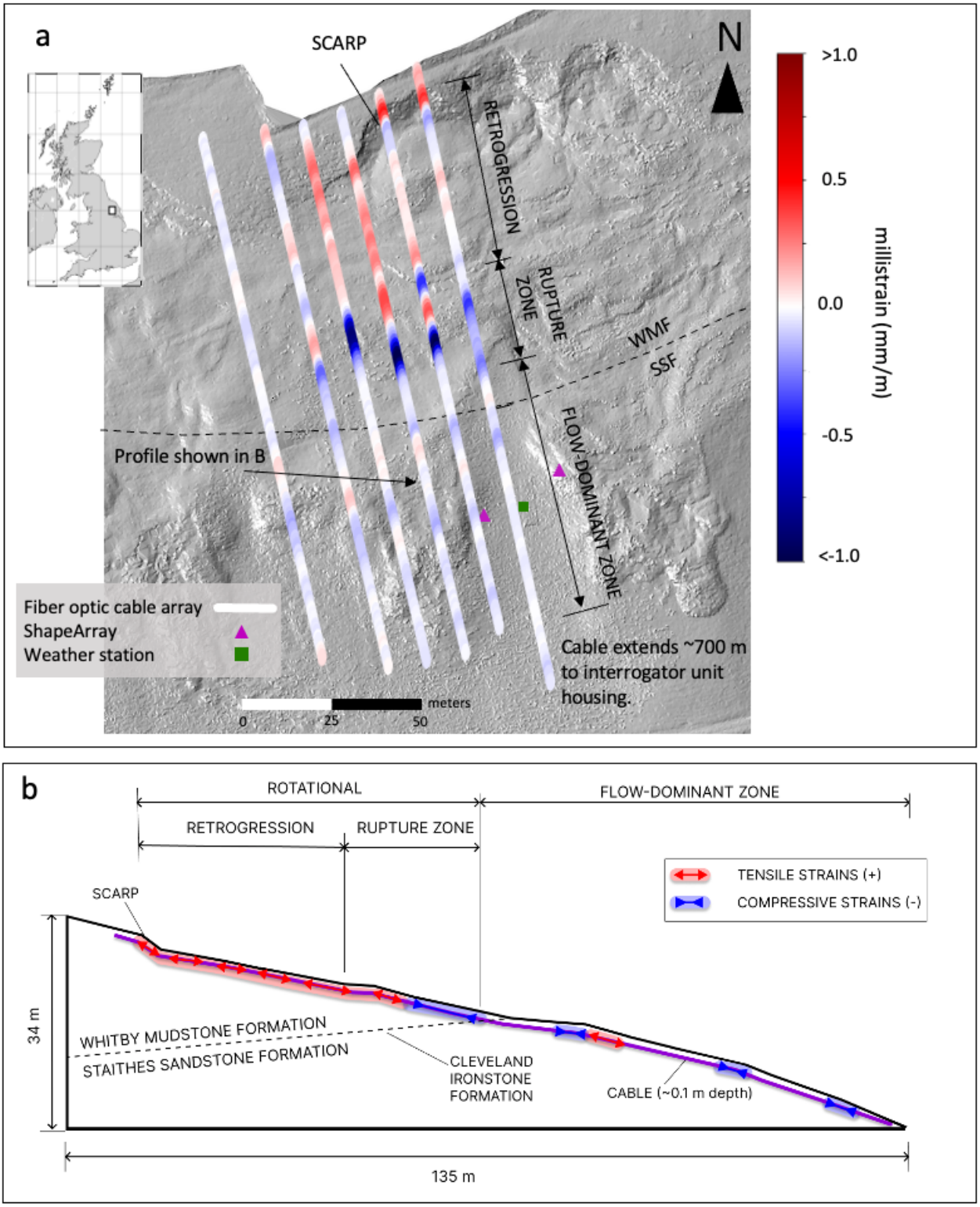

Figure 1

Hollin Hill Landslide Observatory and fiber optic cable array. (**A**) Inset figure shows location of Hollin Hill. Base image from bare-earth lidar from a November 2020 terrestrial lidar scan. The in-situ Whitby Mudstone Formation (WMF), Cleveland Ironstone Formation (CIF) and Staithes Sandstone Formation (SSF) geological boundaries are per . Fiber optic cable array shows processed cable sections. Unprocessed cable sections perpendicular to direction of slope movement not shown. DAS strain change

data corresponding to strain change from 2021-01-12T11:38 (baseline) to 2021-01-15T11:00. Soil moisture content sensor and precipitation gauge are located at the weather station. (**B)** Conceptual model illustrating the main landslide zones and approximate strain changes for same time as in (A). Strain vector lengths are for illustration purposes only and do not represent actual strain magnitudes.

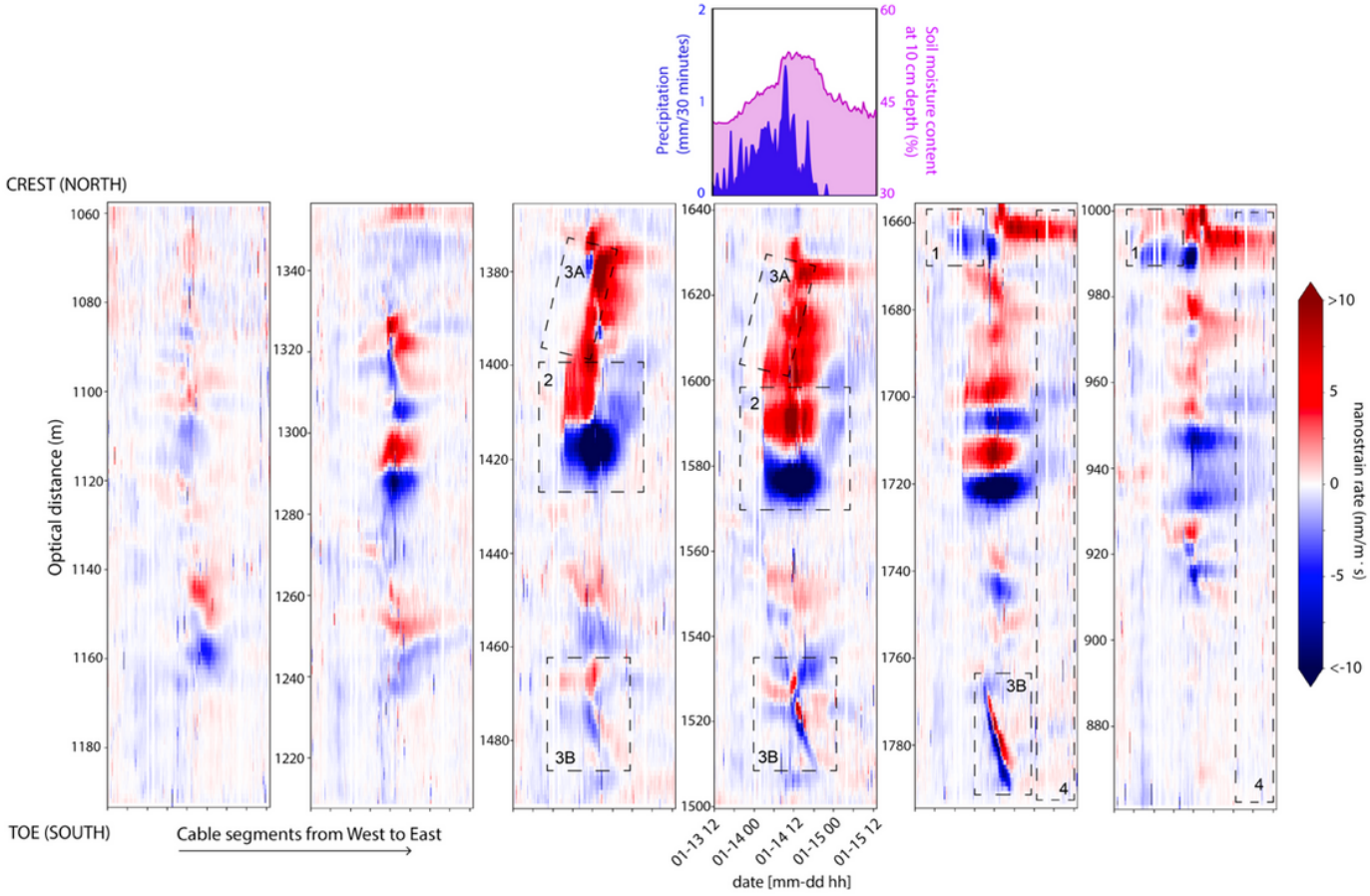

Figure 2

Strain-rate spatiotemporal images at key times of interest. Strain-rate spatiotemporal images along the six cable sections from west (L1) to east (L6). Precipitation and soil moisture content from nearby weather station data shown along same temporal time scale. Dotted grey lines and numbered sequences 1 through 4 correspond with interpretation of observed strain-rate changes described in our results.

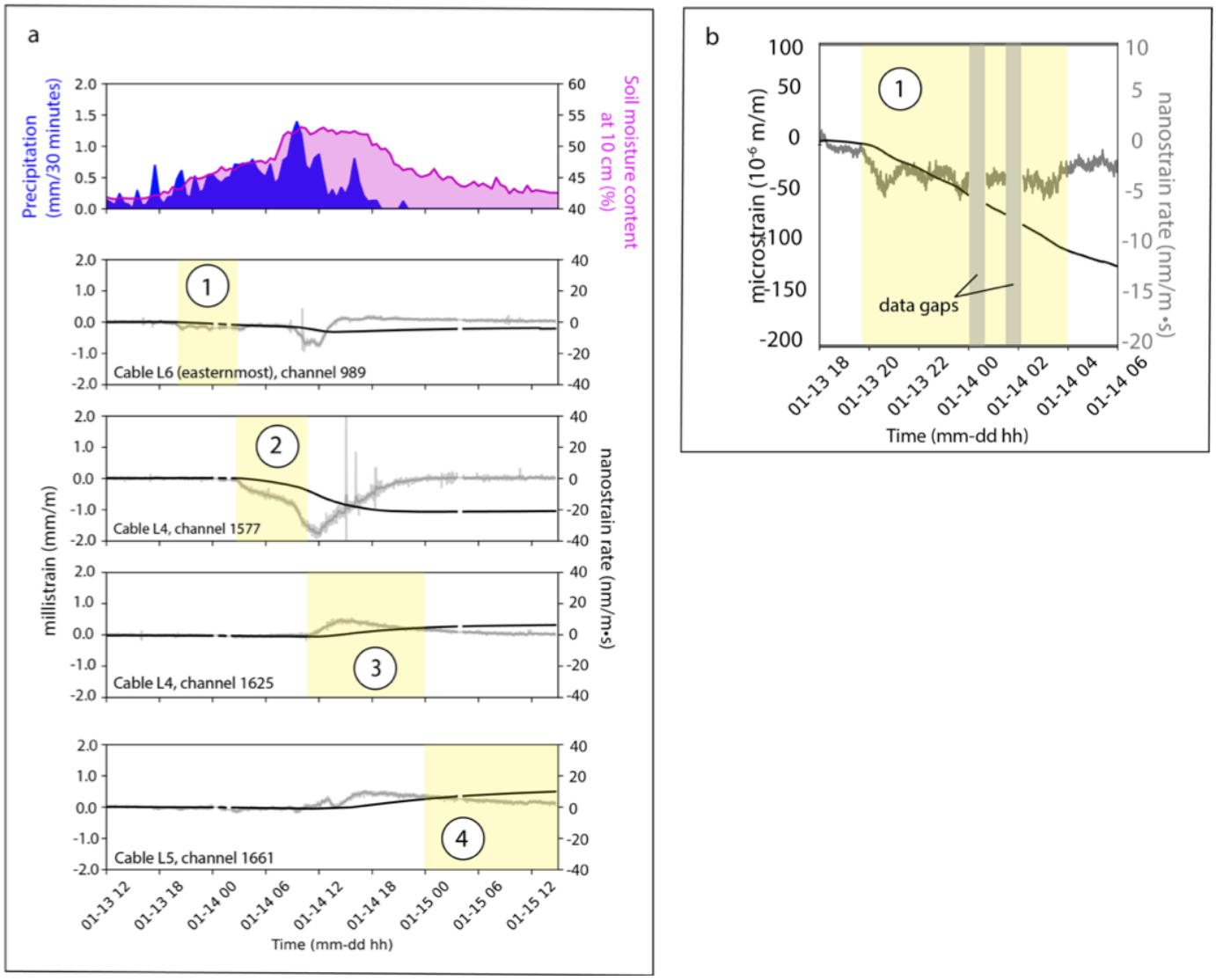

Figure 3

Changes in strain and strain-rate alongside precipitation and soil moisture, with highlighted time periods of interest. (A) Soil moisture content and precipitation data shown alongside strain (black solid line) and strain rate (grey solid line) data at select channels. Approximate channel locations are indicated in **Fig. (6A)** with sequence numbering. Key times of interest are highlighted in yellow. **(B)** Strain and strain-rate at Cable L6, channel 989 to highlight approximate time of strain onset occurring in Sequence 1.

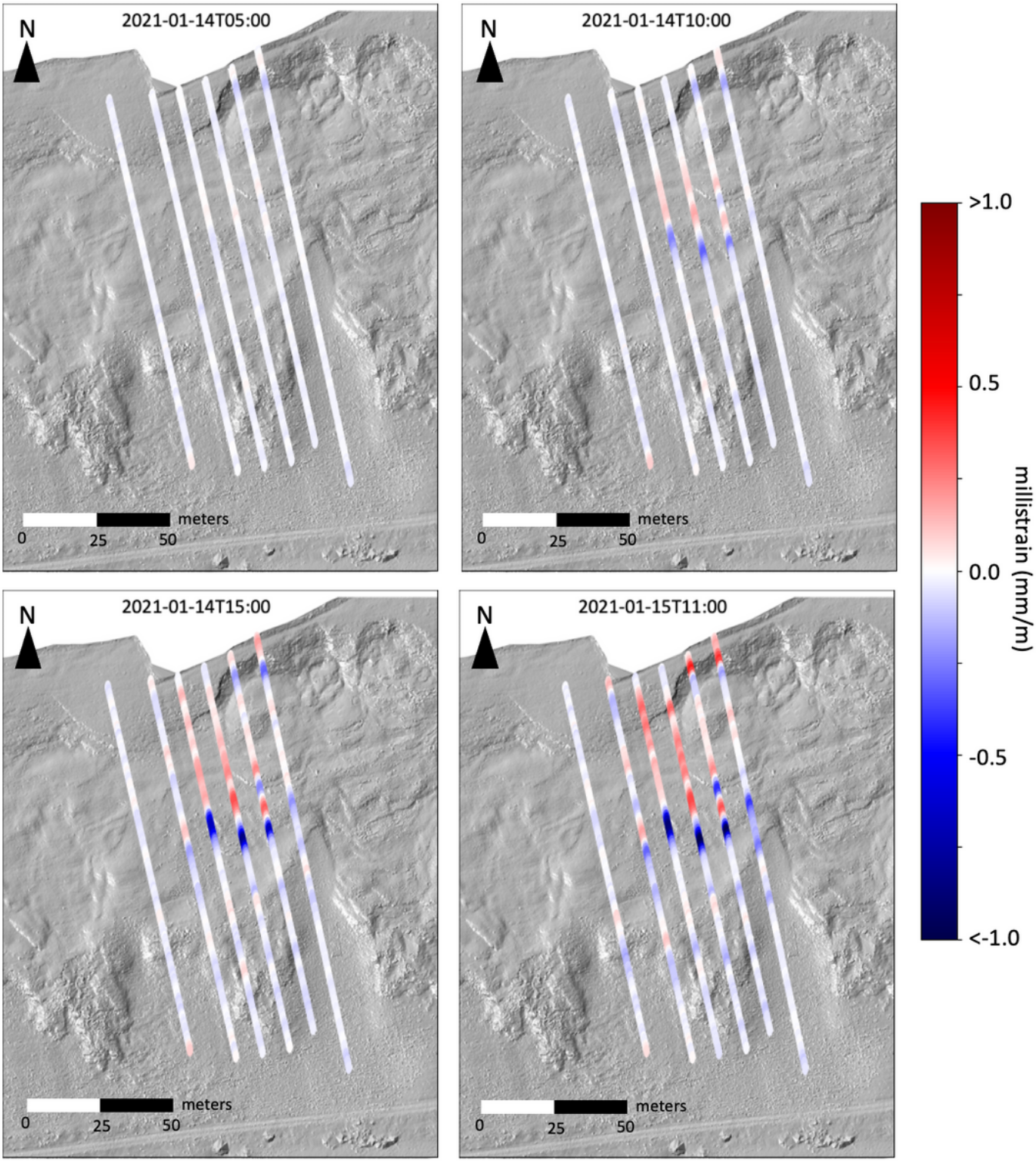

Figure 4

Change in DAS strain at key time periods. Change in strain to illustrate visible changes in strain recorded from DAS data overlain onto lidar bare-earth imagery from November 2020.

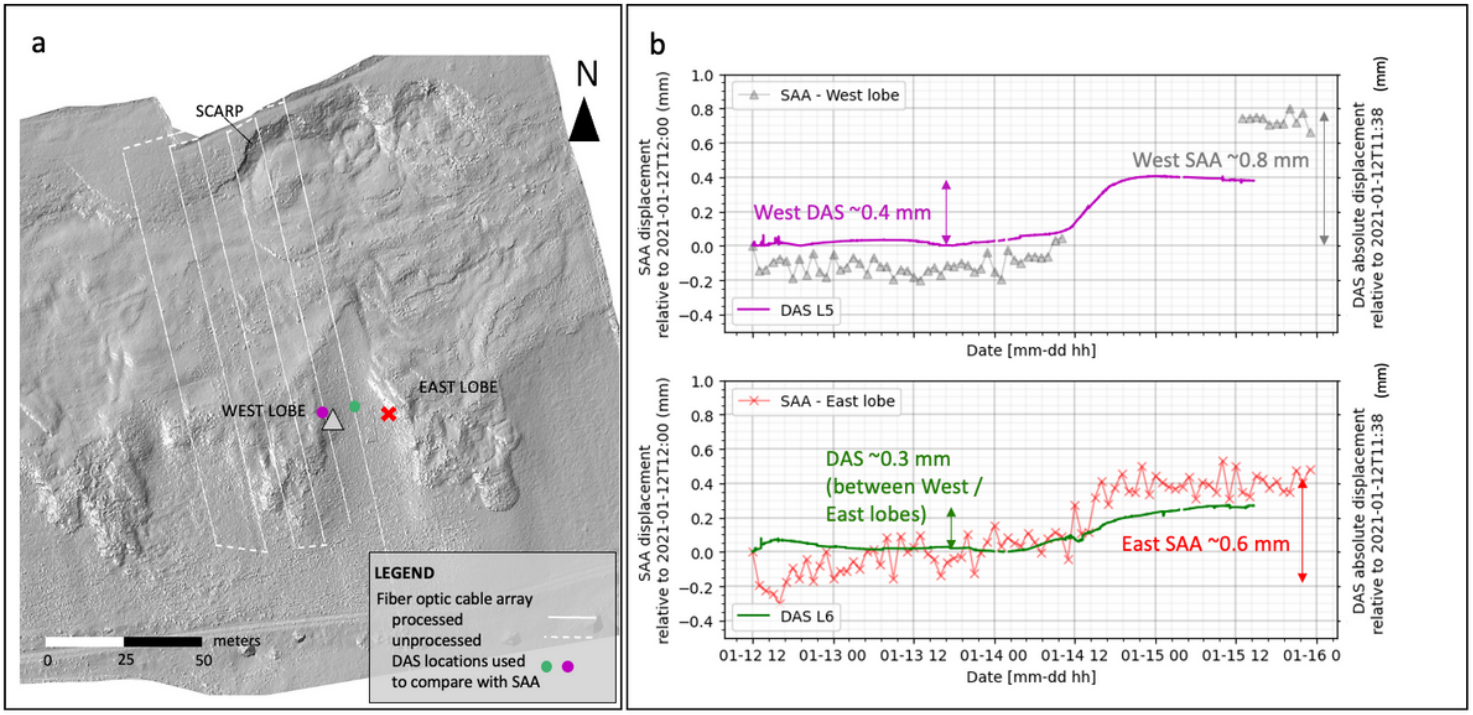

Figure 5

Comparison of ShapeArray displacements with DAS-derived displacements. (A) Overview figure indicating the two DAS channels selected for comparison alongside the location of the two ShapeArrays (SAA), depicted as a grey triangle and red cross on the west and east lobes, respectively. Google Earth Imagery dated May 6, 2020. **(B)** Time displacement plot comparing the DAS-derived displacements with the ShapeArray displacements.

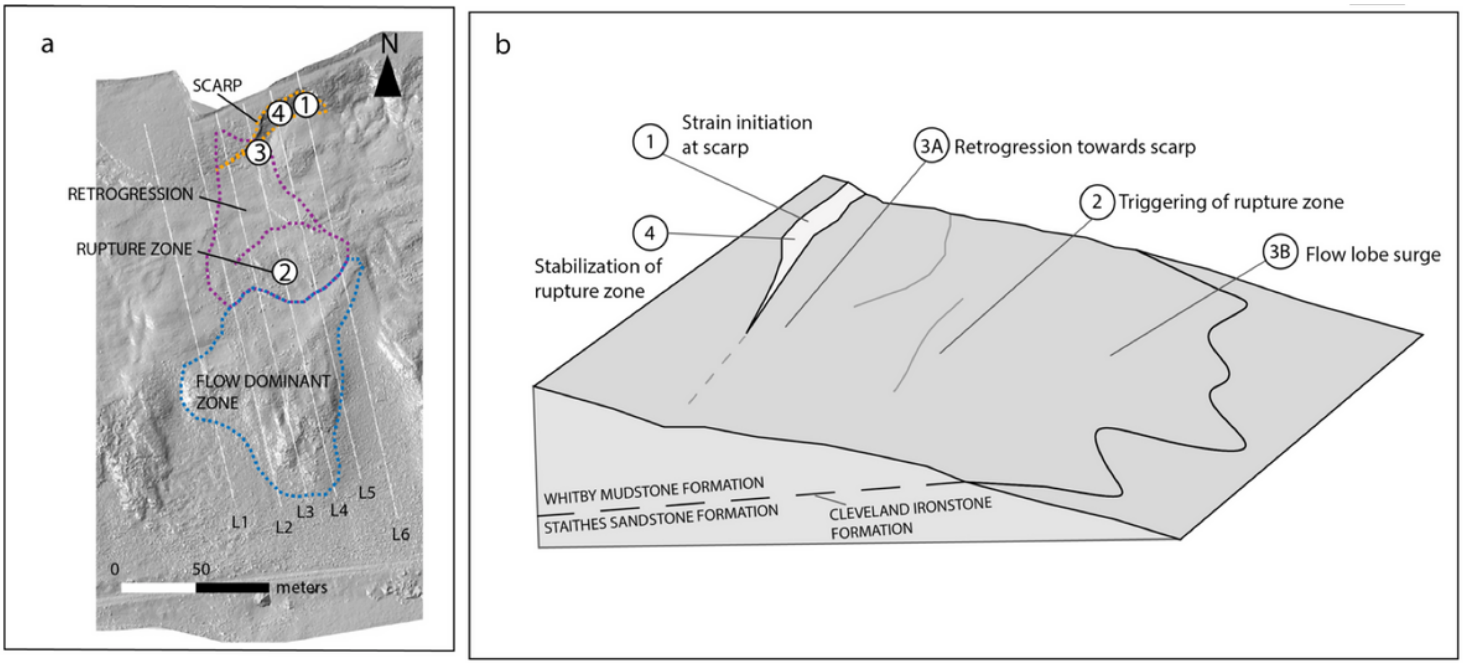

Figure 6

Diagram of landslide zones. (a) Sketch of zones of interest overlain onto bare-earth imagery from November 2020 terrestrial lidar scan. Location of processed fiber optic cable data in white. Approximate channel locations indicated with sequence numbering. **(b)** Simple 3D cartoon schematic to illustrate primary zones of observed strain changes and temporal sequence of events.

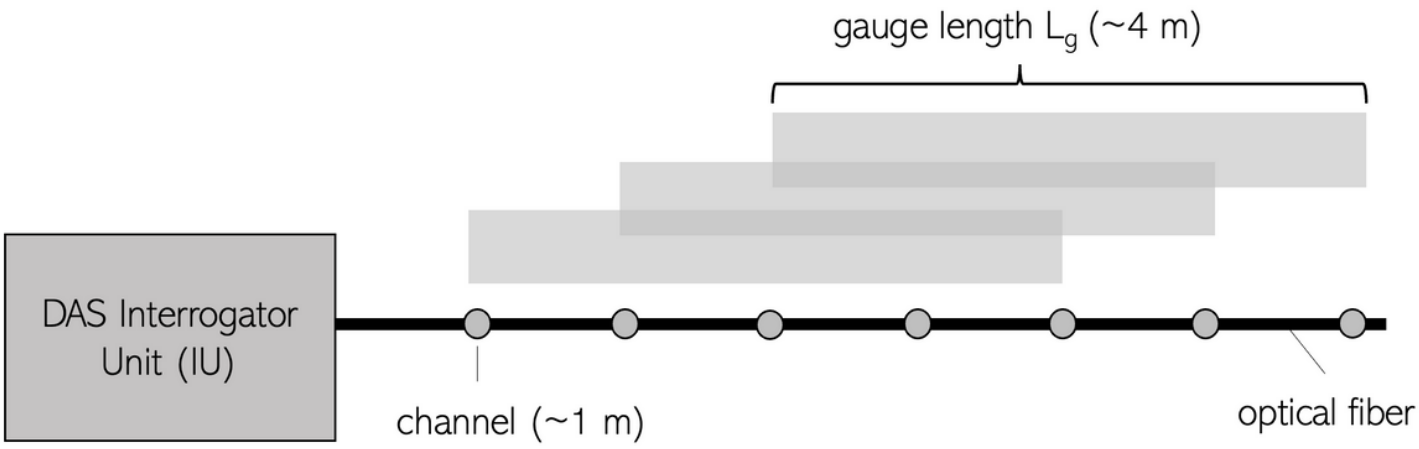

Figure 7

Illustrative diagram of the DAS interrogator unit with the measurement points (channels) and gauge length.

Supplementary Files

This is a list of supplementary files associated with this preprint. Click to download.

- supplementaryfinal.docx